# Accepted Manuscript


## Mercury distribution and speciation in biochar particles reacted with contaminated sediment up to 1030 days: A synchrotron-based study

Peng Liu, Carol J. Ptacek, David W. Blowes, Y. Zou Finfrock

PII: S0048-9697(19)30165-2
DOI: https://doi.org/10.1016/j.scitotenv.2019.01.148
Reference: STOTEN 30462

To appear in: *Science of the Total Environment*

Received date: 22 October 2018
Revised date: 13 January 2019
Accepted date: 13 January 2019

Please cite this article as: Peng Liu, Carol J. Ptacek, David W. Blowes, Y. Zou Finfrock , Mercury distribution and speciation in biochar particles reacted with contaminated sediment up to 1030 days: A synchrotron-based study. Stoten (2018), https://doi.org/10.1016/j.scitotenv.2019.01.148

# Mercury distribution and speciation in biochar particles reacted with contaminated sediment up to 1030 days: A synchrotron-based study

Peng Liu[a,b], Carol J. Ptacek[*, b], David W. Blowes[b], Y. Zou Finfrock[c,d]

[a]*School of Environmental Studies, China University of Geosciences (Wuhan), 388 Lumo Road, Wuhan, 430000, P.R. China*
[b]*Department of Earth and Environmental Sciences, University of Waterloo, 200 University Avenue West, Waterloo, Ontario, Canada N2L3G1*
[c]*Science Division, Canadian Light Source, 44 Innovation Bld., Saskatoon, Saskatchewan, Canada S7N2V3*
[d]*CLS@APS Sector 20, Advanced Photon Source, 9700 South Cass Ave., Argonne, Illinois 60438*

**Abstract**

A previous long-term microcosm experiment showed mercury (Hg) in aqueous phase of contaminated sediment was effectively stabilized through the addition of biochar. The present study focuses on the application of synchrotron-related methods to evaluate the distribution and speciation of Hg in the biochar particles reacted for 235, 387, and 1030 days. The study provided more information on Hg stabilization mechanisms in addition to the information obtained by the previous studies. Confocal micro-X-ray fluorescence imaging (CMXRFI) and micro-X-ray fluorescence (micro-XRF) maps show that mercury co-exists with S, Cu, Fe, Mn, and Zn on the surface and inside the particles of biochar. Extended X-ray absorption fine structure (EXAFS) modeling shows that Hg is in an oxide form on the surface of an iron (hydro)oxide particle from fresh sediment and in Hg-sulfide forms in biochar samples. S X-ray absorption near-edge structure (XANES) analyses show that sulfide is present within the biochar particles. After amendment with biochars, a fraction of the Hg originally present in unstable forms (dissolvable, HgO, colloidal, nano, etc.) in the sediment was likely stabilized as less soluble Hg-sulfide phases

[*] Corresponding author address: Department of Earth and Environmental Sciences, University of Waterloo, 200 University Ave. W., Waterloo, ON, Canada N2L 3G1. Tel: +01 (519) 888 4567, ext. 32230
E-mail: ptacek@uwaterloo.ca

on the surface or within the biochar particle. These results suggest Hg accumulation by the biochar particles renders it less potential for transport and bioavailability.

**Key Words**

Mercury; confocal X-ray micro-fluorescence imaging; biochar; sediment; synchrotron-based techniques

## 1 Introduction

Mercury (Hg) widely distributes in air, oceans, lake, rivers, soils, and sediments and can occur as elemental Hg, as $Hg^{2+}$, in complexes with dissolved organic matter, and in organomercurial forms (Selin, 2009). Organic Hg, e.g. methylmercury (MeHg), is the most toxic form and can cause serious defects to central nervous system (Tchounwou et al., 2003). Hg can be converted from inorganic or elemental to organic forms by microbes (Hu et al., 2013; Zhang et al., 2012). The primary intake pathway of Hg is by the accumulation of dissolved species of Hg by aquatic organisms. The methylation and accumulation of Hg species by organisms is primarily initiated in the aquatic environment, especially in sediments. If Hg can be stabilized and transformed to less soluble, mobile, bioavailable, and bioaccessible forms in sediments, the health risk caused by Hg will be reduced. Laboratory studies show Hg is effectively removed from aqueous solution (Bundschuh et al., 2015; Dong et al., 2013; Liu et al., 2016) and sediment (Gomez-Eyles et al., 2013; Liu et al., 2017a; Liu et al., 2018a; Wang et al., 2019a) using biochars; as such, biochar is a potentially cost-effective reactive material for application in Hg-contaminated site remediation.

Biochar has been used for Hg, other heavy metals and organic pollutants control in sediment and paddy soils (Bussan et al., 2016; Gomez-Eyles et al., 2013; O'Connor et al., 2018; Shu et al., 2016; Wang et al., 2019b; Xiao et al., 2018; Zhang et al., 2018). The current study

combines geochemical aqueous analysis and solid-phase elemental analysis to determine Hg and MeHg distribution among different system phases to delineate the effect of biochar addition on Hg-contaminated media. These analyses are still critical in the future study of Hg stabilization using biochars. However, a knowledge gap exists regarding Hg species transformation and distribution after sediment amendment with biochar. The species or mineral form of Hg determines its stability and bioavailability; for example, Hg in aggregated Hg-S forms is expected to be more stable than other forms including nano-size or colloidal particulates as well as oxides and halogenated species. Moreover, the same Hg species located inside a biochar particle is expected to be more stable and less bioavailable than if present on the surface, where more exposure to the surrounding environment results in more opportunities for direct contact with potential Hg methylators. Advanced techniques are required to characterize the Hg species and spatial distribution during the stabilization process.

Synchrotron radiation-based techniques, including micro-XRF, CMXRFI, XANES, and EXAFS, are advanced tools for investigation of the spatial distribution and local geometric and/or atomic structure of elements of interest (Calvin, 2013; Pushie et al., 2014). For example, micro-XRF and CMXRFI can be used to delineate multiple element distribution at the micrometer scale (Liu et al., 2017a; Liu et al., 2018b; Meng et al., 2014; Nesbitt and Lindsay, 2017), XANES analysis provides the oxidation state (Jamieson-Hanes et al., 2017; Liu et al., 2016), and EXAFS can be used to obtain the chemical state and local coordination of the element of interest (Gibson et al., 2011; Liu et al., 2016; Liu et al., 2018b; Ravel et al., 2009; Skyllberg et al., 2006). These techniques can be used not only for Hg, but also for other elements without considerable extra work. Other elements that are important with respect to Hg speciation and distribution include S, Fe, Cu, and Zn.

We previously described a serious of batch and long-term microcosm experiments designed to investigate aqueous Hg removal and stabilization of Hg in aqueous-sediment mixtures using biochars prepared from a range of different feedstocks (Liu et al., 2016; Liu et al., 2017a; Liu et al., 2018a). The results indicate that Hg can be effectively removed from aqueous solution in batch experiments (Liu et al., 2016); concentrations of Hg in contaminated sediment amended with biochar are lower than in sediment controls without biochar after 30-250 days (Liu et al., 2018a). In this study, we applied synchrotron-related techniques to characterize particles from more biochar types derived from these long-term microcosm experiments (1030 days). The purpose of these analyses is to identify the distribution and speciation of Hg to provide an indication of mechanisms leading to Hg stabilization as well as an explanation for the phenomena observed in aqueous phase analysis. The synchrotron radiation-based techniques employed for this purpose include micro-XRF, CMXRFI, Hg and Cu EXAFS, and S XANES.

## 2 Materials and methods

### 2.1 Microcosm experiment

A 1030-day anaerobic microcosm experiment was conducted by mixing activated carbon or biochars, Hg-contaminated sediment (particle size <3mm), and water at a ratio of 1:20:160 on a dry mass basis in 1 L amber bottles to avoid the effect of light. The biochars included oak biochar (CL2; Cowboy Charcoal Co.) and low-temperature (300 °C; GR4L) and high-temperature (600 °C; GR4H) switchgrass biochars. The size of AC and biochar particle was in the range of 0.1-3 mm. The selection of the biochars was based on the results from previous batch-style experiments (Liu et al., 2015; Liu et al., 2016; Liu et al., 2018c), which showed low (GR4L) and high (AC, CL2, GR4H) Hg removal percentages, low (AC, CL2, GR4H) and high potential (GR4L) to release organic acids and dissolved organic matter, low (CL2) and high potential to release sulfate (AC, GR4L, GR4H). GR4L and GR4H were selected to evaluate

difference in the Hg stabilization potential due to pyrolysis temperature of biochar. Controls included 1) biochar-water mixture and 2) sediment-water mixture at the same ratios as the amended systems.

The amber bottles were placed in an anaerobic chamber over the experimental period at room temperature (25ºC). The system was maintained under anaerobic conditions with Eh values <0 mV after 7 d and < -420 mV after 126 d (Liu et al., 2018a). The bottles were shaken after each sampling event. More details of the experiment were presented in a previous study which focused on the discussion of aqueous phase parameters and microbes in solid phase (Liu et al., 2018a).

**2.2 Solid samples**

The Hg-bearing and sediment particles were collected at days 65, 100, 154, 235, 387, and 1030 with a scoopula. Individual biochar particles were handpicked from the amended system using tweezers, and washed with ultra-pure water. These solid samples were freeze-dried and stored under anaerobic conditions before analysis. The fresh sediment and biochar particles collected at day 387 were frozen-dried and ground into fine powders (<0.1 mm) for total Hg analysis. The powers of 0.1 g were digested using 50 mL aqua regia for 7 d. Triplicate digestion was performed and a chi-square test was performed to evaluate if the measurements are significant different ($P$<0.05). The mixture was filtered using 0.45 μm hydrophilic polyethersulfone filters (Pall Corp., UK). Total Hg concentrations of the filtrates were determined by cold vapor atomic fluorescence spectroscopy (Tekran Instruments).

**2.3 Reference materials and sample preparation for synchrotron analysis**

Reference materials for XAS analyses included cinnabar, metacinnabar, and HgO for Hg; $Cu_2S$, CuS, CuO, and Cu foil for Cu; and cinnabar, elemental S, L-cysteine, dibenzothiophene, Na

methane sulfonate, and $K_2SO_4$ for S. Fine powder of the reference material was prepared and smeared on polyethylene terephthalate tape for collection of Hg and Cu EXAFS. For collection of S XANES spectra, the reference materials were either smeared on double-sided carbon tape for analysis on Sector SXRMB of Canadian Light Source (CLS) using total electron yield mode, or mixed with graphite at 5% content for analysis on Beamline GSECARS at Advanced Photon Source (APS; Lemont, IL) using fluorescence mode. The graphite was used to dilute pure S compounds to decrease the effect of self-adsorption (Jalilehvand, 2006). Methodological details are described in Liu et al. (2016).

Unreacted sediment, particles from the sediment control, and the biochar particles were embedded in epoxy and prepared as thin-sections (Φ=26mm; thickness as 30 μm) for micro-XRF and Hg micro-EXAFS analyses. Bulk samples of unreacted sediment and separated biochar particles were also prepared for Hg EXAFS spectra. Particles of AC and CL2 from biochar controls and the amended systems at day 387 were freeze-dried for bulk S XANES analysis.

**2.4 Micro-XRF maps**

Micro-XRF maps of the thin-sections were collected on 13-IDE and 20-IDB at the APS following the setup and procedures described by Liu et al. (2016). Briefly, a focused 2×2 $\mu m^2$ beam, 2 μm step, and 12.6 keV photon energy were applied for micro-XRF maps. The sample stage and detector was oriented at 45° and 90° to the beam, respectively.

**2.5 Confocal micro-X-ray fluorescence imaging (CMXRFI)**

CMXRFI analysis of biochar particles collected from amended systems reacted for 1030 days was performed on Beamline 20-ID at the APS. A quartz slide (22×22 $mm^2$) was used for particle attachment. The data were collected using the setup and methods described by Liu et al. (2017b). Briefly, the data were collected using 12.6 keV incident energy, ~2×2 $\mu m^2$ beam size, 5 μm step

size, a Ge optical unit, a Si-drift Vortex detector, and an angle between the incident beam and sample holder of 35°. The map was collected in the horizontal plane (*xy* plane) of the particle. The intensities of the XRF and incident beam were corrected for each pixel of the map using the algorithm provided in Liu et al. (2017b). Data processing and plotting were performed in MATLAB®.

### 2.6 XANES and EXAFS

Areas with elevated Hg, Cu, and S intensity indicated by micro-XRF maps were identified for acquisition of micro-EXAFS or micro-XANES spectra. Hg EXAFS spectra of bulk fresh sediment and biochar particles were collected using the same setup as for EXAFS spectra collection of Hg-enriched areas in the thin-sections using unfocused beam. S XANES spectra of bulk biochars from amended systems and controls were collected on the SXRMB beamline.

The EXAFS spectra of Hg and Cu and XANES spectra of S were first processed by Athena, then EXAFS spectra was modeled using Artemis (Ravel and Newville, 2005). The modeling steps followed a previous method (Liu et al., 2018b). Briefly, the weak oscillations of EXAFS spectra was enhanced by a $k^3$ weighting. The amplitude reduction factor ($S_0^2$) and mean-square radial displacement ($\sigma^2$) were obtained by keeping the coordination numbers (*CN*) invariant during refinement of the first and second (only $Cu_2S$) shells for the reference materials. Then, $S_0^2$ and $\sigma^2$ were kept constant during refinement of the first and second shells to obtain the *CN*.

## 3 Results and discussion

### 3.1 Hg contents in fresh sediment and biochars

Total Hg content in the fresh sediment was 186 μg $g^{-1}$ (Fig. 1). The total Hg contents in the biochars reacted with the sediment for 387 day were all greater than that of the fresh sediment with ratios ranged from 3 to 9.3. Greatest total Hg content was observed in GR4L (1730 μg $g^{-1}$),

and least were observed in CL2 (274 μg $g^{-1}$). This observation inversely corresponds to the aqueous total Hg concentration in previous study (Liu et al., 2018a), and explained the decrease of total mercury in aqueous concentration is a result of accumulation in the biochars.

**3.2 XAS analysis of sediment controls**

Micro-XRF map of a fresh sediment particle shows Hg and Cu present on the surface of an Fe-enriched particle (Fig. 2). The Fe-enriched particle is assumed to be an iron (hydro)oxide phase based on microscopic images in reflection and transmission mode (Fig. S1). The Hg and Cu-enriched areas are located within the cavities of this particle. XRF spectra of the arrow-indicated area in the Hg $L_{\alpha}$ line map confirm the existence of Hg in the cavities and show coexistence of Hg, Fe, Cu, and Zn. The maps of a particle from the sediment control at day 235 show coexistence of Hg, Fe, Ni, Cu, and Zn (Fig. 2 and Fig. S2). Whether this Hg-enriched particle was newly formed during the experiment period or was present in the source sediment prior to the experiment is difficult to discern. Attempts were made to collect μ-XRF maps of the two particles at 2.5 keV for S, but the intensity of S was not distinguishable from the background, which indicates the particle was not rich in S.

Hg from the enriched area of the particles of fresh sediment and the sediment control at day 235 is in the Hg oxide form indicated by μ-EXAFS modeling results (Fig. 2 and Table 1), with coordination numbers for the Hg with the O atoms of 2.15 and 4.97 and bond lengths of 1.95 and 2.21 Å, respectively. In contrast, the EXAFS of bulk fresh sediment (fine or colloidal fraction) indicate the Hg is primarily present as metacinnabar (β-HgS) with a coordination number of 3.07 for the Hg with the S and a bond length of 2.51 Å. The modeling results indicate Hg is present as a Hg oxide in the enriched area and Hg in the sediment is primarily in a Hg

sulfide form, consistent with Hg sequential extraction results (Fig. S3) and in agreement with previous studies (Gibson et al., 2015; Lowry et al., 2004).

The observation of Hg on the surface of a (hydro)oxide phase in the natural sediment and coexistence of Hg with Mn, Fe, and Cu (in oxide form; Supporting Information) are consistent with observations from previous studies at Hg-contaminated sites (Bernaus et al., 2006; Gibson et al., 2015; Gu et al., 2014). Hg can be effectively adsorbed by iron (hydro)oxide by forming bidentate inner-sphere complexes on the substrate surface (Collins et al., 1999; Kim et al., 2004). The Hg from the Hg-enriched area of fresh sediment is in a Hg-oxide form with a coordination number of 2.15 and bond length of 1.95 Å, which are consistent with Hg EXAFS modeling results for Hg(II) sorption onto goethite (Kim et al., 2004).

**3.3 Micro-XRF maps of biochar particles**

The distribution of Hg, Cu, Fe, and S is indicated by the micro-XRF maps for four particles of AC and biochars collected from the amended Hg-contaminated sediment at day 387 (Fig. 3). The micro-XRF mapping indicates Hg coexists with S, Cu (in $Cu_2S$ form in AC-387 and CL2-235&387; in Cu(0) in another CL2-387; SI), Fe, Mn, and Zn, whereas Ni-enriched areas are located in separate spots of the particle pores (Fig. 3 and Fig. S5-S17). The distribution patterns of Hg, Cu, Fe, and S are different for these particles: for AC, these elements not only distributes on the surface but also penetrate into the particles; for CL2, the elements are primarily located in two large pores, other small pores, and the edges of the particle; for low-T switchgrass biochar (GR4L), the Hg, Fe, and Cu are primarily located inside the particle; and for high-T switchgrass biochar (GR4H), the most Hg, Cu, and Fe are observed on the surface and inside the pores of the particle. These observations are based on the microscopic images collected under transmission mode (Fig. S16-S17).

Biochar particle thin-sections from day 65, 154, and 235 were also prepared for μ-XRF map, but Hg XRF intensity was low and poor quality μ-XRF maps were obtained for the majority of the thin sections. The likelihood of locating Hg-enriched biochar particles increased as the experiment continued past 235 days. The results indicate limited Hg accumulation by AC and the biochars at the beginning of the experimental period. This observation is consistent with the total Hg concentration changes in the aqueous phase (Liu et al., 2018a), which demonstrate an increase and then a decrease in total Hg concentrations in the amended systems. The increase of aqueous Hg concentration is likely due to the reduction of Fe(III) minerals, which results in the release of Hg into solution (Liu et al., 2018a). The decrease in Hg concentration occurs after the sulfate reduction period, which indicates the stabilization of Hg is achieved by Hg-S mineral formation.

The results indicate that Hg coexists with Cu, Fe, and S on surface, inside the pores, or inside the particles of AC and biochars. The difference in element spatial distribution of different biochar type is likely due to the following reasons: 1) different porous structure, e.g. biochar with macro pores (>70 nm (Zdravkov et al., 2007), even >10 μm (Figs. 3&4)), AC without macro pores (Laine and Yunes, 1992); 2) pore types (accessibility for metal accumulation), e.g. closed or open pores, pores open at one end or both ends (Zdravkov et al., 2007); 3) penetrability in the structure material or the skeleton (Liu et al., 2017a). The distribution of Hg in the GR4L and GR4H systems is consistent with the results from other particles from the same experiment (Liu et al., 2017a). Due to the stability of biochar (Spokas, 2010), the Hg that co-exists with these elements could be stable for prolonged periods. Furthermore, the Hg is located and aggregated within the coarse biochar particles, potentially lessening its bioavailability.

**3.4 Confocal micro-X-ray fluorescence imaging**

CMXRFI analysis was conducted for AC and biochar particles from the amended systems reacted for 1030 days (Fig. 4 and Figs. S18-21). The porous structure of the particles is indicated by the Ca intensity maps, because Ca is a common element in the feedstock (plant) of AC and the biochars. The distributions of Mn, Co, Ni, Cu, and Zn are similar to Fe for each particle (Fig. S18-21), and therefore Fe was selected to prepare the tricolor plot in combination with Ca and Hg (Fig. 4). The distributions of S, Fe, and Hg for all particles are not identical, but show similar trends. Fe and Hg distribute across the AC particle, but primarily accumulate on the surface of the structural material (e.g., pore walls). Fe and Hg primarily distribute on the surface of CL2 and GR4H. For GR4L, Fe and Hg distribute across the profile and localized inside the structural material, in contrast to on the surface of pore walls for AC or only on the particle surface for CL2 and GR4H.

The step size for CMXRFI analysis was 5 μm in both the horizontal (*y* axis) and depth (*x* axis) directions (Fig. 4). The maps indicate features are distinguishable at this resolution (5 μm), especially for Fe and Hg maps. While the thickness of the thin section was 30 μm, the signal received by the detector for micro-XRF analysis was 42 μm (30 μm/*sin*(45°), considering the geometry of the setup). This length was the same as the medium pore space in GR4L (Fig. 4). This calculation indicates the micro-XRF maps show the elemental distribution over a thickness of 42 μm, but the CMXRFI maps show features are distinguishable at a resolution of 5 μm. Therefore, CMXRFI analysis provides more precise elemental distribution and pore structure information compared to micro-XRF results, consistent with a previous study applying micro-XRF and CMXRFI to an archaeological bone (Choudhury et al., 2017).

The CMXRFI analysis indicates Hg was still accumulated on the surface of the particle or pore wall for CL2, GR4H, and AC even after 1030 days. However, for GR4L, Hg distributes

inside the structural material. Results from the microcosm study indicate the lowest total MeHg and Hg concentrations in GR4L-amended system and suggest GR4L is the best candidate for sediment Hg stabilization (Liu et al., 2017a; Liu et al., 2018a). The distribution of Hg inside the structural material of GR4L is likely one of the reasons for the lowest total aqueous Hg and MeHg concentrations. The encapsulation of Hg inside the GR4L particle results in more stable and less bioavailable forms of Hg. For other reactive materials, Hg distributes on the surface of the particle or pore walls; this Hg that is still exposed to the surrounding environment is not as stable as Hg located inside the structure of the biochar particle.

**3.5 S XANES**

S XANES spectra were collected for standards and samples (Figs. 5 and S22). The energies of lines 1-6 are 2471.9, 2472.7, 2473.5, 2474.3, 2481.4, and 2482.8 eV, respectively. These lines were obtained from spectra collected from the standards corresponding to inorganic-sulfide, elemental, thiol, thiophenic, sulfonate, and ester-sulfate sulfur functionalities, respectively, following the assignment from Manceau and Nagy (2012 and Vairavamurthy (1998. The S XANES spectra collected for AC and CL2 particles from control and amended systems at day 387 display a number of edge features that indicate different S forms are present.

Thiophenic S (line 4) and ester-sulfate S (line 6) structures are observed in all spectra, but their relative intensities are low for the thin-section spot of the AC-amended system. The elemental S (line 2) structure is observed in the thin-section spot of the CL2-amended system and bulk samples of the AC control and amended systems. The bulk spectra from the amended system are more complex than those from the biochar control in which reactive media was only mixed with river water; sulfonate (line 5) is only obvious in the amended systems.

The differences between the spectra of bulk samples and the spectra of thin-section spots from the amended systems indicate the S species are highly heterogeneous; the sulfonate S peak is more pronounced than the ester-sulfate peak, and the thiol S (line 3) peak is only observed in a thin-section spot of the AC amended system. The shoulder indicated by line 1 in the thin-section spots of AC and CL2 amended systems is at a similar energy as the S peak of cinnabar (Fig. S22).

The spectra of AC and CL2 controls at day 387 are similar to the corresponding washed samples (Liu et al., 2016), which indicate the S forms in AC and CL2 are relatively stable under the experimental conditions. Differences between the amended systems and controls are likely due to the sediment matrix. During the experiment period, sulfate is released from the biochar and sediment (Liu et al., 2016; Liu et al., 2018a), and sediment is expected to release more sulfate because the mass of the sediment was 20 times of the biochar, the S content of the sediment is greater than those of the biochar, and limited sulfate is released from these biochars in a previous batch-style experiment (Liu et al., 2016). Sulfate concentration decreased from 28 mg $L^{-1}$ to <detection limit in the aqueous phase (Liu et al., 2018a), which indicates sulfate was reduced by sulfate-reducing bacteria to generate sulfide. The reduced sulfur then co-precipitates with other elements, e.g., Fe, Cu, Hg, on the surface or in the pores of the amended reactive materials (Figs. 3 and S18-S21). The sulfate or other oxidized S forms undergo a series of reactions and are finally converted to carbon-bonded sulfide, thiol, and sulfonate forms at the end of the experimental period.

**3.6 Hg EXAFS for biochar particles**

Hg EXAFS data were obtained from the thin-section enriched areas, and the bulk AC and biochars reacted with the sediment (Fig. 6 and Fig. S4). The results show Hg is likely in cinnabar (α-HgS) form in the enriched spots of AC, CL2, GR4L and GR4H particles (Fig. 3; Table 1), and

another five enriched areas from CL2 particles (Figs. S6, 9, 11-13 and Table S1). The modelled coordination numbers (CN) of S range from 1.00 to 2.88 and modelled bond lengths range from 2.36 to 2.38 Å for Hg-enriched area (Table 1), in agreement with cinnabar (Fig. S23 and Table S2) and previous studies (Bisson et al., 2012; Gibson et al., 2011; Li et al., 2012; Liu et al., 2016). The EXAFS results are in accordance with the S XANES spectra (Fig. 5) of the spots collected from the Hg-enriched area (Fig. 3). For bulk biochar samples reacted with the contaminated sediment for 387 days, the Hg is primarily present as newly formed cinnabar form for CL2 and GR4L with Hg coordination numbers of 2.54 and 1.93 and bond lengths of 2.32 and 2.36 Å, respectively (Table 1). The Hg is primarily present as metacinnabar (β-HgS) for AC and GR4H bulk samples with coordination numbers of 3.91 and 3.24 and bond lengths of 2.55 and 2.49 Å, respectively, which are close to the metacinnabar reference material (Fig. S23 and Table S2); this observation is different from the Hg-enriched area of the corresponding thin-sections. This difference indicates the fraction of the Hg species from the enriched area were too low to be accounted in the bulk sample. Hg in methyl form may also be in the biochar particle, but methyl Hg was not observed by the analysis of EXAFS likely due to its low fraction (usually<0.1% of total Hg (Qiu et al., 2005)).

The XAS and Hg sequential extraction analyses of the fresh sediment indicate the presence of Hg on the surface of iron (hydro)oxide particles as Hg-oxide and soluble forms of Hg, and the majority of Hg in the sediment in fine particles and in Hg sulfide forms (Fig. 2 and Fig. S3). The synchrotron-based results show the coexistence of Hg, Fe, Cu, and S on the surface or inside the particles of AC and biochars and that the Hg is in Hg-sulfide forms. The Hg in the bulk AC and biochar samples is also in Hg-sulfide forms. Based on the results, the Hg observed in the AC and biochar particles is likely converted from soluble forms of Hg, Hg released during

dissolution of iron (hydro)oxide, and Hg from colloidal or nano particles; this Hg interacts with biogenic sulfide converted from sulfate by sulfate-reducing bacteria to form Hg sulfide. These results are consistent with the process described in Liu et al. (2018a) and provide direct evidence for the evolution observed in the aqueous phase. The EXAFS results are also consistent with the observations from micro-XRF and CMXRFI results (Figs. 3 and 4). The difference between Hg speciation in bulk sample and Hg-enriched area indicate the Hg removal mechanisms involve multiple processes, but the primary process was the formation of Hg sulfide species.

**4 Conclusions**

The results of this study indicate part of the Hg in the contaminated sediment is converted to Hg sulfide that co-exists with S, Fe, Cu, and Zn after amendment with activated carbon, oak wood and switchgrass biochar particles. The biochar particles likely provide a host for Hg to accumulate in sulfide forms indicated by micro-XRF (17 particles), CMXRFI (9 particles), Hg EXAFS and S XANES analyses, with the Hg being stabilized in these particles compared to its original forms (soluble forms, colloidal, nano, or fine particles). The biochar particles did not decompose and were distinguishable after 1030 days. Biochars can be stable in natural environments for prolonged periods; co-occurrence of Hg with biochar particles could therefore also lead to increased stability of Hg over the long term. Low-temperature biochar is likely the most promising biochar, as Hg was observed in the form of Hg sulfide minerals and distributed across the particle and located in the structural material.

Biochar particles are fragile and light, and therefore can be physically broken down and transported by flowing water. Because biochar particles are enriched in Hg, this process potentially facilitate the transport of Hg to the downstream of the river. Engineering controls is required to keep the biochar particles in shape and in place. The present study simulated the

situation that after amending sediment with biochar the exchange of the pore water with surface water or groundwater is limited, for example due to the formation of new layer of sediment on the top of the mixture or a clay layer under the loose sediment. Full-scale applications for site remediation is required to be evaluated.

**Acknowledgments**

This study was funded by E. I. du Pont de Nemours and Company, Natural Sciences and Engineering Research Council (NSERC) from Canada, Program of Geological Processes, Resources and Environment in the Yangtze Basin (No.: CUGCJ1702), and the National Natural Science Foundation of China (No.: 41877478). Synchrotron analysis was conducted at Sectors 13-ID and 20-ID at Advanced Photon Source and at SXRMB of Canadian Light Source. We are thankful for advice from Science Team of South River, F. Budimir, J. Jamieson-Hanes, H. Shrimpt, A. Wang, Y. Hu, J. Dyer, M. Newville, Y. Liu, and R. Parigi.

## References


Bernaus A, Gaona X, Esbrí JM, Higueras P, Falkenberg G, Valiente M. Microprobe techniques for speciation analysis and geochemical characterization of mine environments: the mercury district of Almadén in Spain. Environ. Sci. Technol. 2006; 40: 4090-4095.

Bisson TM, MacLean LCW, Hu Y, Xu Z. Characterization of mercury binding onto a novel brominated biomass ash sorbent by X-ray absorption spectroscopy. Environ. Sci. Technol. 2012; 46: 12186-12193.

Bundschuh M, Zubrod JP, Seitz F, Newman MC. Effects of two sorbents applied to mercury-contaminated river sediments on bioaccumulation in and detrital processing by *Hyalella azteca*. J. Soils Sediments 2015; 15: 1265-1274.

Bussan DD, Sessums RF, Cizdziel JV. Activated carbon and biochar reduce mercury methylation potentials in aquatic sediments. Bull. Environ. Contam. Toxicol. 2016; 96: 536-539.

Calvin S. XAFS for Everyone. New York: CRC Press, Taylor & Francis, 2013.

Choudhury S, Agyeman-Budu DN, Woll AR, Swanston TM, Varney T, Cooper DM, et al. Superior spatial resolution in confocal X-ray techniques using collimating channel array optics: elemental mapping and speciation in archaeological human bone. J. Anal. At. Spectrom. 2017; 32: 527-537.

Collins CR, Sherman DM, Ragnarsdottir KV. Surface complexation of $Hg^{2+}$ on goethite: mechanism from EXAFS spectroscopy and density functional calculations. J. Colloid Interface Sci. 1999; 219: 345-350.

Dong X, Ma LQ, Zhu Y, Li Y, Gu B. Mechanistic investigation of mercury sorption by Brazilian pepper biochars of different pyrolytic temperatures based on X-ray photoelectron spectroscopy and flow calorimetry. Environ. Sci. Technol. 2013; 47: 12156-12164.

Gibson B, Ptacek C, Blowes D, Daugherty S. Sediment resuspension under variable geochemical conditions and implications for contaminant release. J. Soils Sediments 2015; 15: 1644-1656.

Gibson BD, Ptacek CJ, Lindsay MBJ, Blowes DW. Examining mechanisms of groundwater Hg(II) treatment by reactive materials: an EXAFS study. Environ. Sci. Technol. 2011; 45: 10415-21.

Gomez-Eyles JL, Yupanqui C, Beckingham B, Riedel G, Gilmour C, Ghosh U. Evaluation of biochars and activated carbons for *in situ* remediation of sediments impacted with organics, mercury, and methylmercury. Environ. Sci. Technol. 2013; 47: 13721-13729.

Gu B, Mishra B, Miller C, Wang W, Lai B, Brooks SC, et al. X-ray fluorescence mapping of mercury on suspended mineral particles and diatoms in a contaminated freshwater system. Biogeosciences Discuss. 2014; 11: 7521-7540.

Hu H, Lin H, Zheng W, Tomanicek SJ, Johs A, Feng X, et al. Oxidation and methylation of dissolved elemental mercury by anaerobic bacteria. Nat. Geosci. 2013; 6: 751-754.

Jalilehvand F. Sulfur: Not a "silent" element any more. Chem. Soc. Rev. 2006; 35: 1256-1268.

Jamieson-Hanes JH, Shrimpton HK, Veeramani H, Ptacek CJ, Lanzirotti A, Newville M, et al. Evaluating zinc isotope fractionation under sulfate reducing conditions using a flow-through cell and in situ XAS analysis. Geochim. Cosmochim. Acta 2017; 203: 1-14.

Kim CS, Rytuba JJ, Brown Jr GE. EXAFS study of mercury(II) sorption to Fe- and Al-(hydr)oxides: I. Effects of pH. J. Colloid Interface Sci. 2004; 271: 1-15.

Laine J, Yunes S. Effect of the preparation method on the pore size distribution of activated carbon from coconut shell. Carbon 1992; 30: 601-604.

Li X, Lee JY, Heald S. XAFS characterization of mercury captured on cupric chloride-impregnated sorbents. Fuel 2012; 93: 618-624.

Liu P, Ptacek CJ, Blowes DW, Berti WR, Landis RC. Aqueous leaching of organic acids and dissolved organic carbon from various biochars prepared at different temperatures. J. Environ. Qual. 2015; 44: 684-695.

Liu P, Ptacek CJ, Blowes DW, Finfrock YZ, Gordon RA. Stabilization of mercury in sediment by using biochars under reducing conditions. J. Hazard. Mater. 2017a; 325: 120-128.

Liu P, Ptacek CJ, Blowes DW, Finfrock YZ. A beam path-based method for attenuation correction of confocal micro-X-ray fluorescence imaging data. J. Anal. At. Spectrom. 2017b; 32: 1582-1589.

Liu P, Ptacek CJ, Blowes DW, Gould WD. Control of mercury and methylmercury in contaminated sediments using biochars: a long-term microcosm study. Appl. Geochem. 2018a; 92: 30-44.

Liu P, Ptacek CJ, Blowes DW, Landis RC. Mechanisms of mercury removal by biochars produced from different feedstocks determined using X-ray absorption spectroscopy. J. Hazard. Mater. 2016; 308: 233-242.

Liu P, Ptacek CJ, Elena KMA, Blowes DW, Gould WD, Finfrock YZ, et al. Evaluation of mercury stabilization mechanisms by sulfurized biochars determined using X-ray absorption spectroscopy. J. Hazard. Mater. 2018b; 347: 114-122.

Liu P, Ptacek CJ, Blowes DW. Mercury complexation with dissolved organic matter released from thirty-six types of biochar. Bull. Environ. Contam. Toxicol. 2018c: 10.1007/s00128-018-2397-2.

Lowry GV, Shaw S, Kim CS, Rytuba JJ, Brown GE. Macroscopic and microscopic observations of particle-facilitated mercury transport from New Idria and Sulphur Bank mercury mine tailings. Environ. Sci. Technol. 2004; 38: 5101-5111.

Manceau A, Nagy KL. Quantitative analysis of sulfur functional groups in natural organic matter by XANES spectroscopy. Geochim. Cosmochim. Acta 2012; 99: 206-223.

Meng B, Feng X, Qiu G, Anderson CWN, Wang J, Zhao L. Localization and speciation of mercury in brown rice with implications for pan-Asian public health. Environ. Sci. Technol. 2014; 48: 7974-7981.

Nesbitt JA, Lindsay MBJ. Vanadium geochemistry of oil sands fluid petroleum coke. Environ. Sci. Technol. 2017; 51: 3102-3109.

O'Connor D, Peng T, Zhang J, Tsang DC, Alessi DS, Shen Z, et al. Biochar application for the remediation of heavy metal polluted land: A review of in situ field trials. Sci. Total Environ. 2018; 619: 815-826.

Pushie MJ, Pickering IJ, Korbas M, Hackett MJ, George GN. Elemental and chemically specific X-ray fluorescence imaging of biological systems. Chem. Rev. 2014; 114: 8499-8541.

Qiu G, Feng X, Wang S, Shang L. Mercury and methylmercury in riparian soil, sediments, mine-waste calcines, and moss from abandoned Hg mines in east Guizhou province, southwestern China. Appl. Geochem. 2005; 20: 627-638.

Ravel B, Newville M. ATHENA, ARTEMIS, HEPHAESTUS: data analysis for X-ray absorption spectroscopy using IFEFFIT. J. Synchrotron Radiat. 2005; 12: 537-541.

Ravel B, Slimmer SC, Meng X, Wong GCL, Lu Y. EXAFS studies of catalytic DNA sensors for mercury contamination of water. Radiation Physics and Chemistry 2009; 78: S75-S79.

Selin NE. Global biogeochemical cycling of mercury: a review. Annu. Rev. Environ. Resour. 2009; 34: 43-63.

Shu R, Wang Y, Zhong H. Biochar amendment reduced methylmercury accumulation in rice plants. J. Hazard. Mater. 2016; 313: 1-8.

Skyllberg U, Bloom PR, Qian J, Lin CM, Bleam WF. Complexation of mercury(II) in soil organic matter: EXAFS evidence for linear two-coordination with reduced sulfur groups. Environ. Sci. Technol. 2006; 40: 4174-4180.

Spokas KA. Review of the stability of biochar in soils: predictability of O:C molar ratios. Carbon Manag. 2010; 1: 289-303.

Tchounwou PB, Ayensu WK, Ninashvili N, Sutton D. Environmental exposure to mercury and its toxicopathologic implications for public health. Environ. Toxicol. 2003; 18: 149-175.

Vairavamurthy A. Using X-ray absorption to probe sulfur oxidation states in complex molecules. Spectrochim. Acta A Mol. Biomol. Spectrosc. 1998; 54: 2009-2017.

Wang AO, Ptacek CJ, Blowes DW, Gibson BD, Landis RC, Dyer JA, et al. Application of hardwood biochar as a reactive capping mat to stabilize mercury derived from contaminated floodplain soil and riverbank sediments. Sci. Total Environ. 2019a; 652: 549-561.

Wang Y, Dang F, Zheng X, Zhong H. Biochar amendment to further reduce methylmercury accumulation in rice grown in selenium-amended paddy soil. J. Hazard. Mater. 2019b; 365: 590-596.

Xiao X, Chen B, Chen Z, Zhu L, Schnoor JL. Insight into multiple and multi-level structures of biochars and their potential environmental applications: A critical review. Environ. Sci. Technol. 2018.

Zdravkov BD, Čermák JJ, Šefara M, Janků J. Pore classification in the characterization of porous materials: A perspective. Cent. Eur. J. Chem. 2007; 5: 385-395.

Zhang T, Kim B, Levard C, Reinsch BC, Lowry GV, Deshusses MA, et al. Methylation of mercury by bacteria exposed to dissolved, nanoparticulate, and microparticulate mercuric sulfides. Environ. Sci. Technol. 2012; 46: 6950-8.

Zhang Y, Liu Y-R, Lei P, Wang Y-J, Zhong H. Biochar and nitrate reduce risk of methylmercury in soils under straw amendment. Sci. Total Environ. 2018; 619–620: 384-390.

**Table 1.** Best-fit results for the Hg $L_{III}$-edge data from bulk and enriched area of micro-XRF maps of sediment control (SRD) and biochar amended systems.

| Sample | Model | Path | CN | R (Å) | $S_0^2$ | $\sigma^2$ (Å$^2$) | R-factor |
|---|---|---|---|---|---|---|---|
| Fresh SRD_ Bulk | β-HgS | Hg-S | 3.07±0.29 | 2.51±0.01 | 0.718[a] | 0.009[a] | 0.01 |
| Fresh SRD_M6 | HgO | Hg-O | 2.15±1.04 | 1.95±0.03 | 0.962[a] | 0.005[a] | 0.003 |
| SRD-C-235_M6 | HgO | Hg-O | 4.97±1.14 | 2.21±0.03 | 0.962[a] | 0.005[a] | 0.06 |
| AC-387_M1 | α-HgS | Hg-S | 2.88±0.70 | 2.38±0.05 | 0.841[a] | 0.005[a] | 0.04 |
| CL2-387_M1 | α-HgS | Hg-S | 1.00±0.23 | 2.36±0.10 | 0.841[a] | 0.005[a] | 0.02 |
| GR4L-387_M1 | α-HgS | Hg-S | 1.41±0.27 | 2.41±0.03 | 0.841[a] | 0.005[a] | 0.18 |
| GR4H-387_M1 | α-HgS | Hg-S | 1.43±0.62 | 2.41±0.08 | 0.841[a] | 0.005[a] | 0.18 |
| AC-387_Bulk | β-HgS | Hg-S | 3.91±0.53 | 2.55±0.02 | 0.718[a] | 0.009[a] | 0.04 |
| CL2-387_Bulk | α-HgS | Hg-S | 2.54±0.62 | 2.32±0.04 | 0.841[a] | 0.005[a] | 0.18 |
| GR4L-387_Bulk | α-HgS | Hg-S | 1.93±0.14 | 2.36±0.01 | 0.841[a] | 0.005[a] | 0.01 |
| GR4H-387_Bulk | β-HgS | Hg-S | 3.24±0.70 | 2.49±0.03 | 0.718[a] | 0.009[a] | 0.17 |

R-factor represents fitting statistic. [a] values obtained from reference materials (Fig. S18 and Table S2)

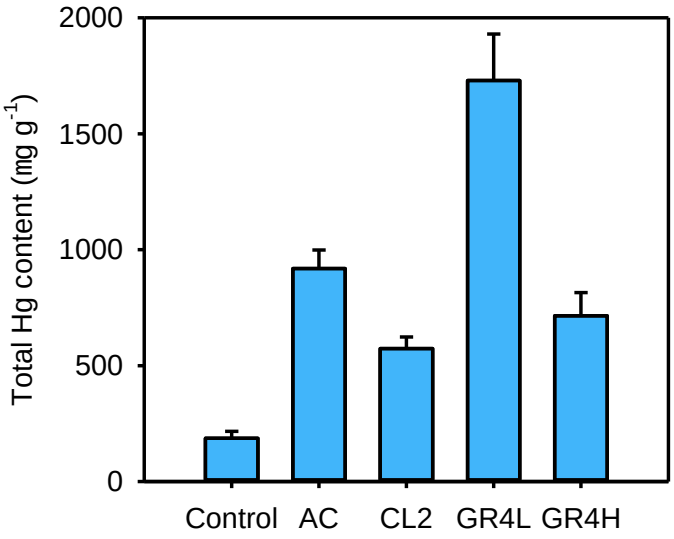


**Figure 1**. The total Hg contents in control (fresh sediment) and activated carbon and biochar reacted with the sediment for 387 d. The triplicate analyses were not significant different ($P$<0.05).

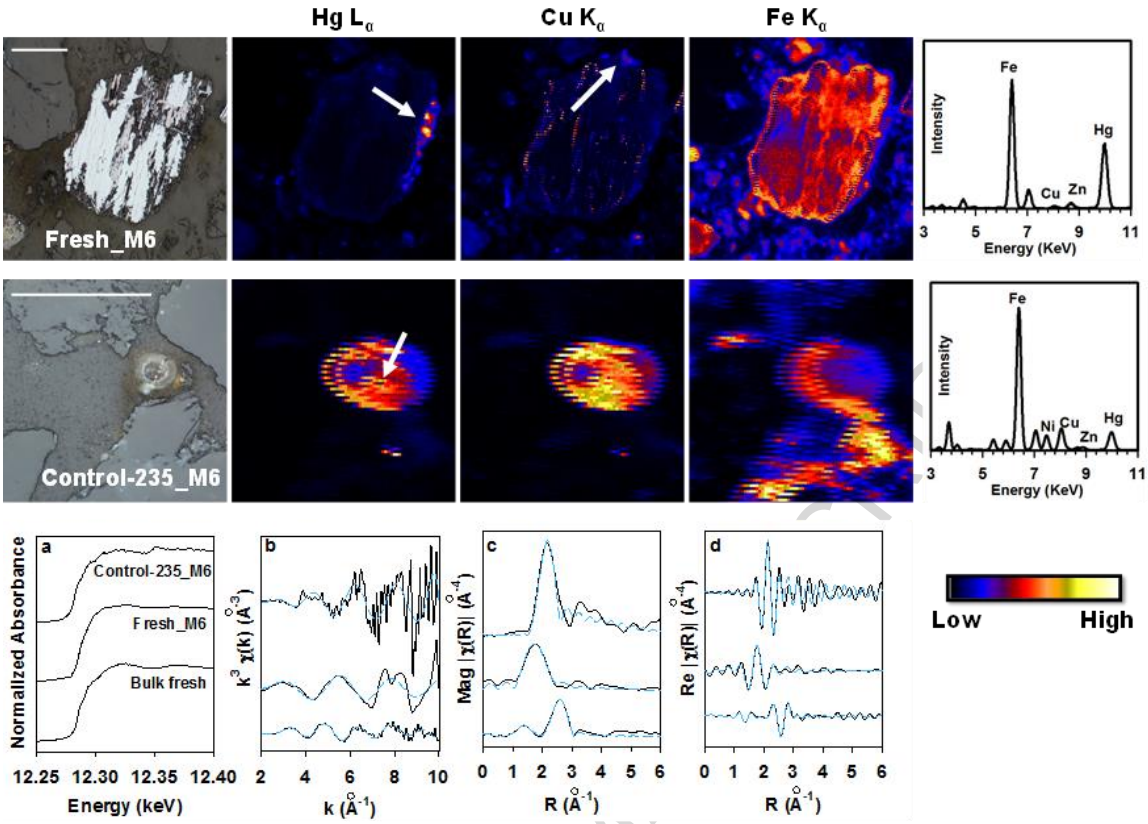


**Figure 2.** Micro-XRF maps of particles from fresh sediment and sediment control at day 235. The first column of the first two rows is the microscopic pictures and the right column is the Hg XRF spectra from the arrow-indicated area. The white line represents 100 µm. The points indicated by the white arrow in Hg and Cu maps indicate Hg and Cu EXAFS spectra were collected. The bottom row includes: a) Normalized absorption data of the spots indicated in the micro-XRF maps and bulk fresh sediment. b) Background-subtracted $\chi(k)k^3$ (black-solid line) and model. c) Magnitude and the model of the Fourier transform (corrected for phase shift). d) Real part and the model of the Fourier transform.

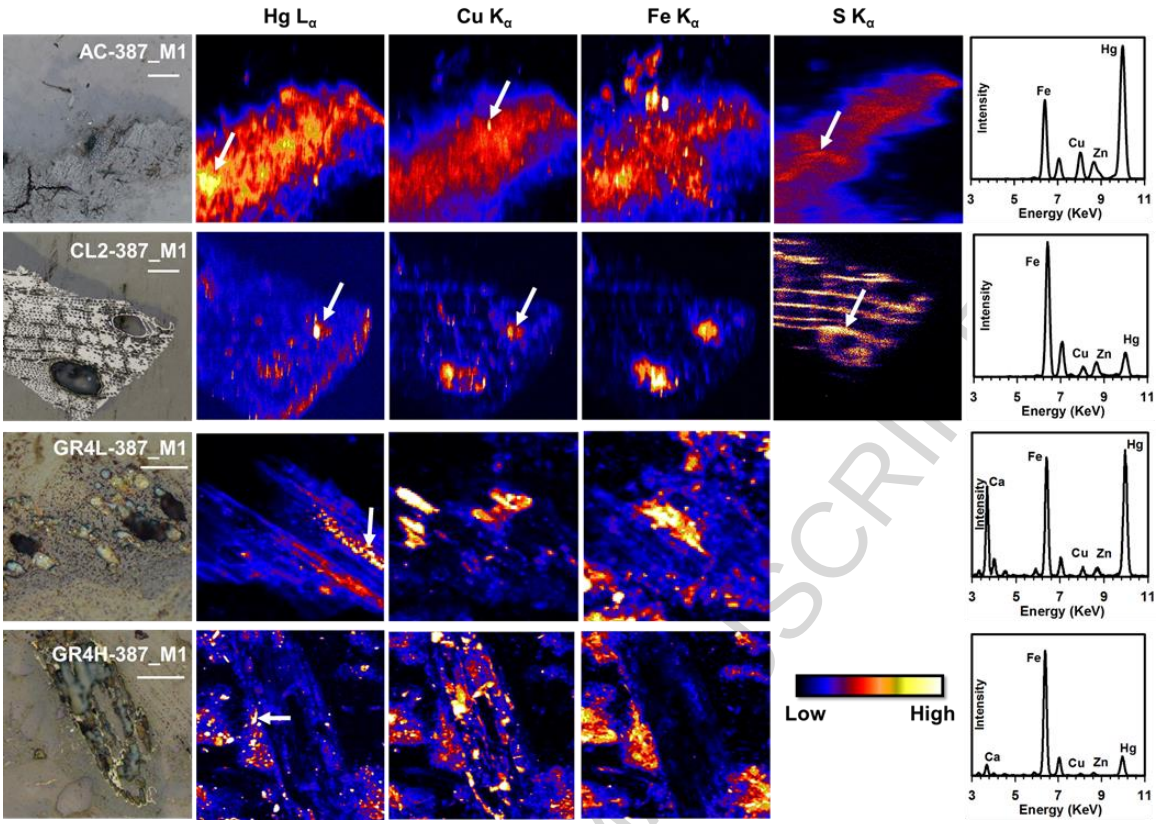


**Figure 3.** Micro-XRF maps of AC, CL2, GR4L, and GR4H from the amended systems reacted for 387 days. The first column is the microscopic pictures and the right column is the Hg XRF spectra from the white arrow indicated area. The white line represents 100 μm. The white-arrow indicated points in the Hg, Cu, and S maps show Hg and Cu EXAFS and S XANES spectra were collected. S XRF maps were collected at different beamlines.

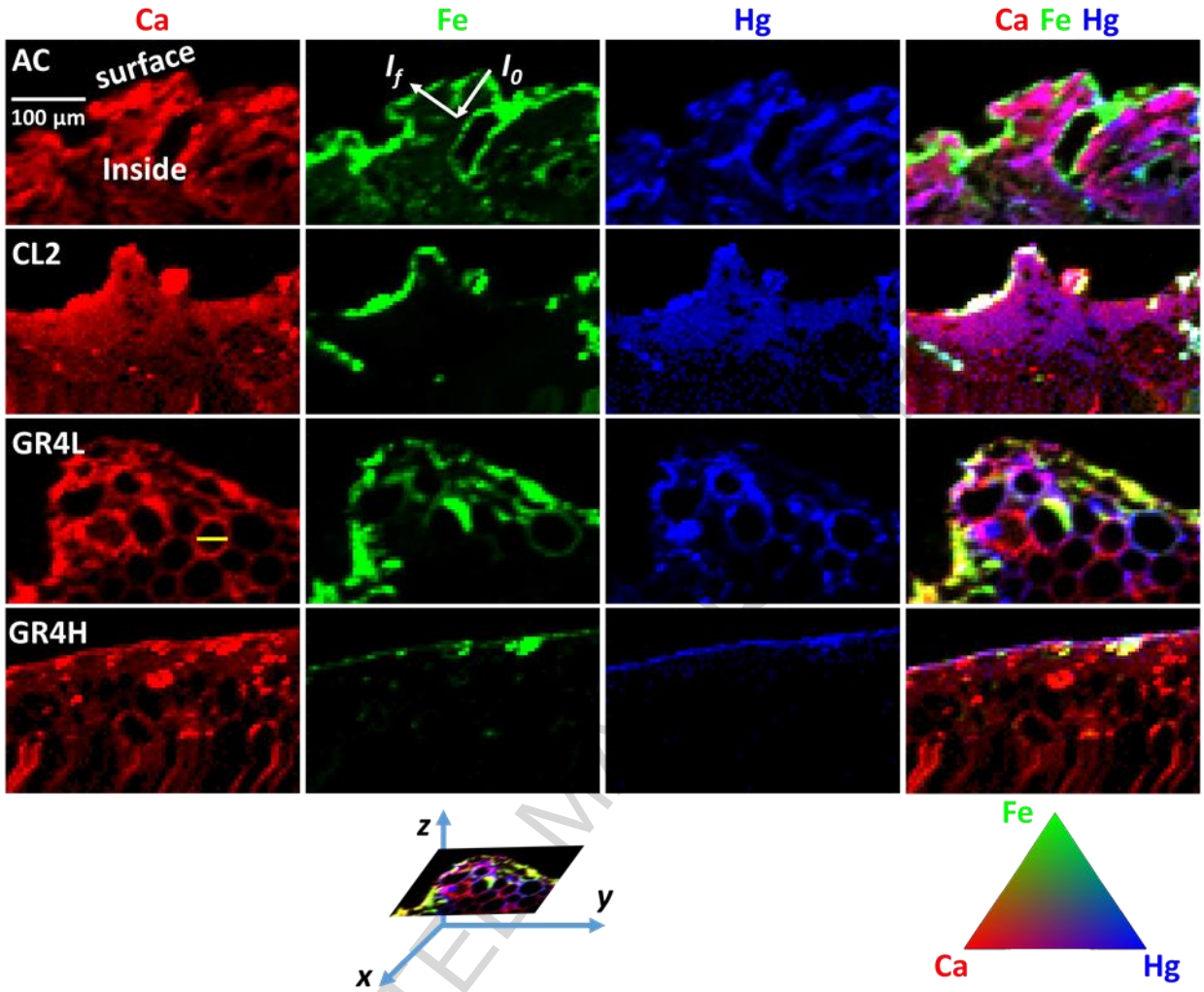


**Figure 4.** Tri-color maps (left to right column: Ca, Fe, Hg, and combination of these elements) obtained using confocal micro-X-ray fluorescence imaging (CMXRFI) of activated carbon (AC) and biochar particles (CL2, GR4L, and GR4H) from the sediment-amended systems at day 1030. The intensity maps were collected in the *xy* plane. The white line represents 100 µm. The yellow line in the Ca intensity map of GR4L represents 42 µm. The incident X-ray ($I_0$) and emitted XRF ($I_f$) paths are indicated by the arrows.

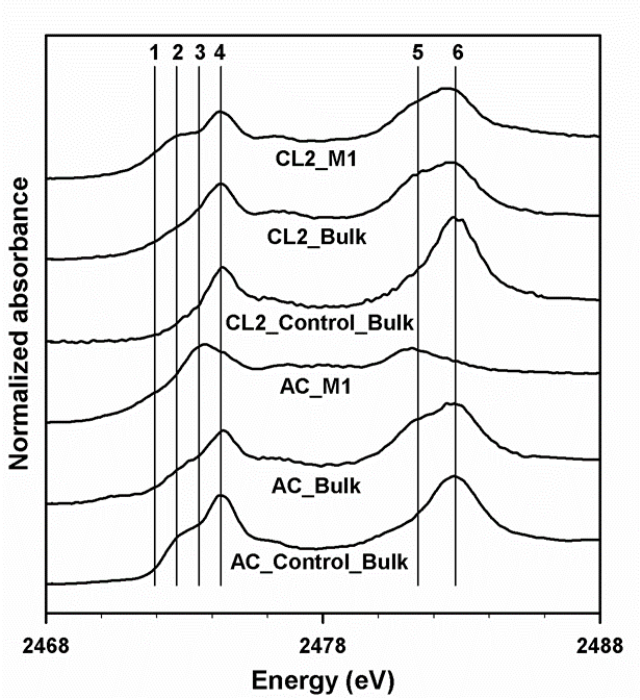


**Figure 5.** S XANES spectra of activated carbon (AC) and CL2 particles from amended systems and control at day 387. *Bulk* represents results of bulk sample analysis. *M1* represents the spectra from spots on thin-sections. S forms indicated by lines 1-6 are inorganic-sulfide, elemental, thiol, thiophenic, sulfonate, and ester-sulfate sulfur, respectively, as assigned by Manceau and Nagy (2012 and Vairavamurthy (1998.

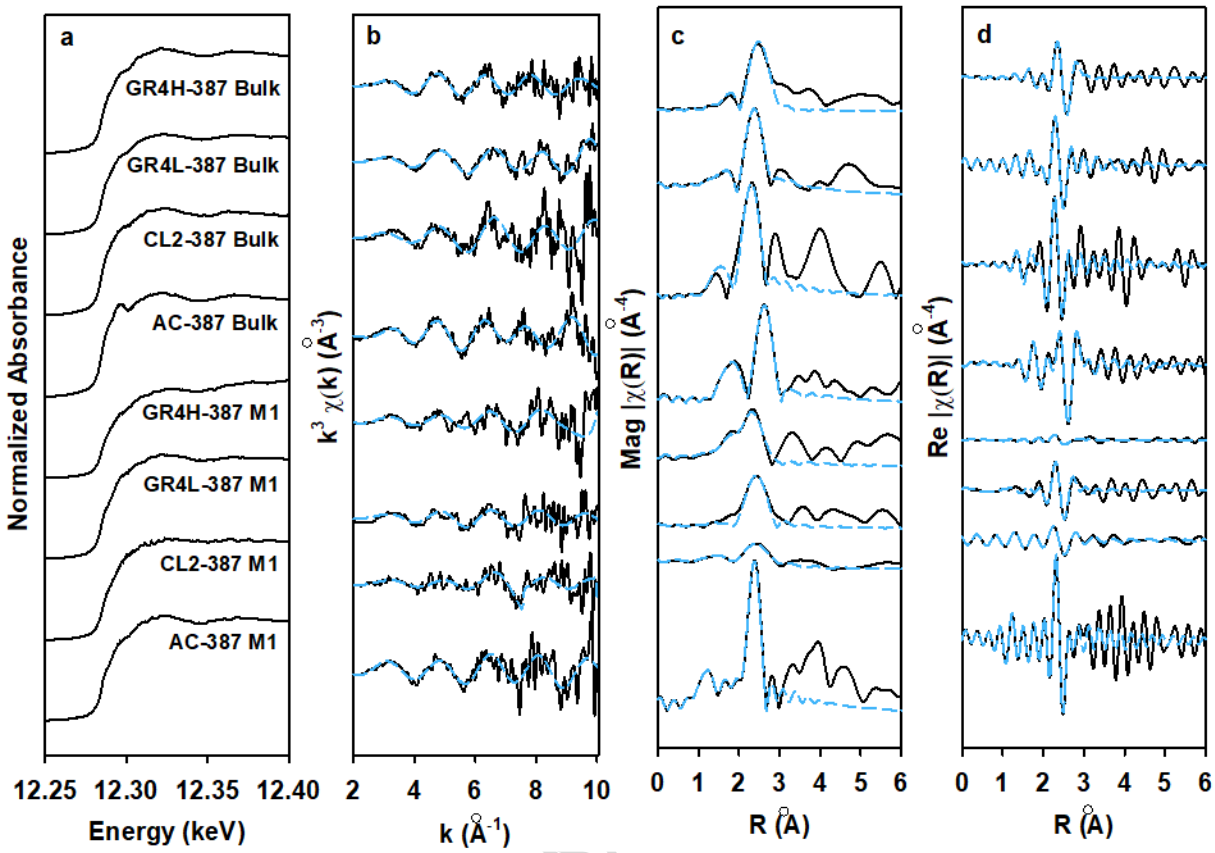


**Figure 6.** Hg $L_{III}$-edge data from bulk sample and enriched area (represented by *M1*) in the µ-XRF maps. a) Normalized absorption data. b) Background-subtracted $\chi(k)k^3$ (black-solid line) and model. c) Magnitude and the model of the Fourier transform (corrected for phase shift). d) Real part and the model of the Fourier transform.

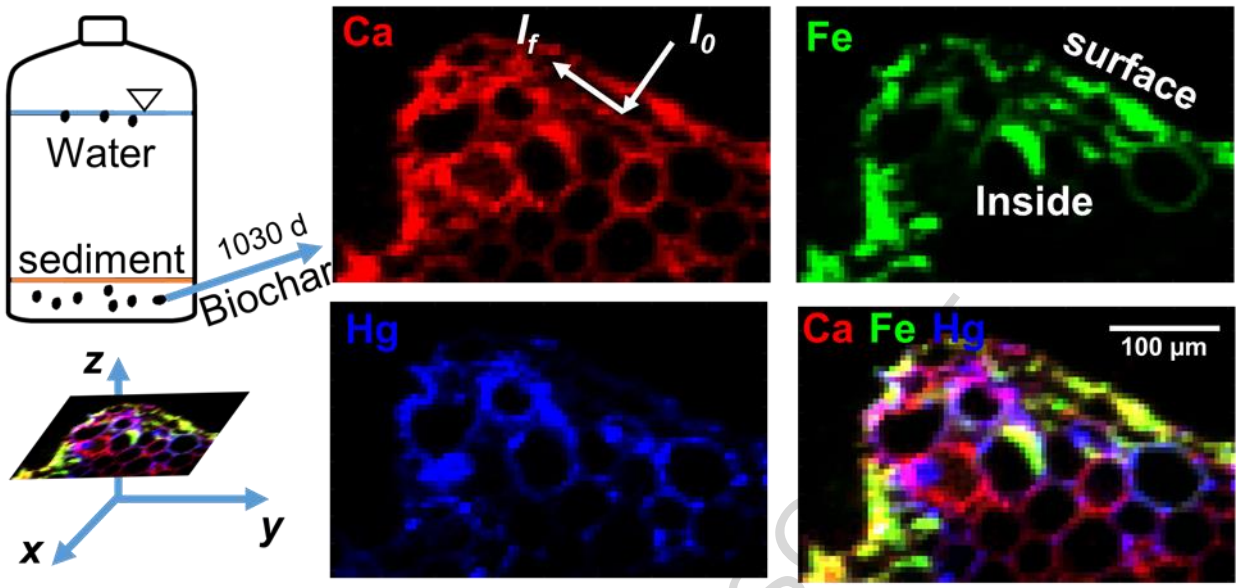


Graphical abstract

Highlights

- Synchrotron-related methods were used to characterize Hg stabilization mechanisms
- Hg is on the surface of an Fe(III)-rich particle in fresh sediment and in Hg-O form
- Confocal micro-XRF shows Hg co-exists with S, Fe, and Cu across biochar particles
- Hg EXAFS analyses show Hg is in sulfide forms in biochars
- S XANES analyses show sulfide is present within the biochar particles